Supporting Information for "River delta morphotypes emerge from multiscale characterization of shorelines"

L. Vulis[1,2], A. Tejedor[1,3], H. Ma[1,4], J. H. Nienhuis[5], C. M. Broaddus[1,6], J.

Brown[6], D. A. Edmonds[6], J. C. Rowland[2], E. Foufoula-Georgiou[1,7]

[1]Department of Civil and Environmental Engineering, University of California, Irvine, CA 92697

[2]Earth and Environmental Sciences Division, Los Alamos National Laboratory, Los Alamos, NM 87545

[3]Department of Science and Engineering, Sorbonne University Abu Dhabi, UAE

[4]State Key Laboratory of Hydroscience and Engineering, Tsinghua University, Beijing, China 100084

[5]Department of Physical Geography, Utrecht University, Utrecht, NL 3584CB

[6]Department of Earth and Atmospheric Sciences, Indiana University, Bloomington, IN 47405

[7]Department of Earth System Science, University of California, Irvine, CA 92697

————

Corresponding author: L. Vulis, Department of Civil and Environmental Engineering, University of California Irvine, Interdisciplinary Science and Engineering Building Room 3400, Irvine, CA 92612, USA. (lvulis@uci.edu).

,

Contents of this file

Additional Supporting Information (Files uploaded separately)

Introduction The Supporting Information for this manuscript includes a detailed description of the methods used for shoreline characterization, discussion on the use of the curvature operator for mapping shorelines to 1-D spatial-series, assessment of the morphometric classification sensitivity to the definition of the fine scale variance, and tabulated values of the morphometrics and sediment flux data.

,

Text S1. Extended Methodology

Shoreline Extraction

The Opening Angle Method (OAM; (Shaw et al., 2008)) was used to define the shorelines of the deltas under study. The OAM and related methods (Geleynse et al., 2012) are used in river mouth impacted coastlines where the traditional definition for a shoreline as the land water interface is not meaningful as the interface can extend far upstream of the actual river mouth.

To utilize the OAM, it is first necessary to generate a binary water mask of the subaerial extent of the delta. Water masks were generated from the Landsat-derived Global Surface Water (GSW) dataset, which provides 30-m spatial and monthly temporal resolution water masks from 1984 to 2018 and is available via Google Earth Engine (Pekel et al., 2016). An individual water mask was used for each delta. In order to account for missing data due to cloud cover and seasonal heterogeneity in water cover, water masks were generally obtained by thresholding the 1984 to 2018 occurrence product, which measures the fraction of time a pixel was covered by water from 1984 to 2018. In deltas with active shorelines e.g. the Danube or Wax Lake, the occurrence for a single representative year was used (Table S1), i.e. maps which measure the fraction of time a pixel was covered by water for a specific year. In the Arctic, snowmelt-driven floods from April to June lead to significant seasonal variability in inundation and apparent subaerial delta extent, therefore the June occurrence was used to identify maximum mouth extent (Vulis et al., 2021). When necessary, masks were manually cleaned to edit or remove features such as jetties or rice paddies, which are visible from contemporaneous satellite imagery

,

and the GSW has difficulty accounting for at its 30-m spatial resolution. Lastly, the OAM algorithm computes an opening angle on all water pixels that lie within the convex hull of the land in the water mask, which leads to unnecessary computations in channel sections upstream of the mouth which are entirely blocked by land. Therefore, these upstream sections were manually marked as land which decreased OAM runtime, as has been previously proposed (Baumgardner, 2016). The OAM was then run on the water mask corresponding to each delta. We made computational improvements to the OAM which significantly improved runtime, and have published this as an R package available via GitHub (https://github.com/lvulis/ROAM). A critical angle θ_c of 45° was then used to define the shoreline as an ordered set of coordinates $S_{45}^R : \{(x,y)_{45}\}$, although we found that the emergent shoreline classification does not change when using a critical angle θ_c of 50°. The shoreline defined in S_{45}^R only extends over the subaerial extent of the delta with start and end points of the shoreline defining the limits of the delta. The subaerial delta was visually outlined and compared with geologic maps where the extent was not clear from Landsat imagery. Note that in several deltas, non-depositional sections of the coastline were included in S_{45}^R, e.g. in valley confined systems such as the Dnieper and Don, and these were removed. Also note that the Missisippi Head of Passes, the Atchafayla, and Wax Lake deltas were all analyzed as separate systems due to their spatial independence in line with other studies (Galloway, 1975; Geleynse et al., 2012; Konkol et al., 2022; Knights et al., 2020).

Finally, to remove discretization artifacts on the shorelines which arise from being defined at the 30-m pixel scale, the raw shoreline in S_{45}^R was first smoothed using a Nadaraya-

,

Watson kernel smoother with a bandwidth of 180-meters (Strimas-Mackey, 2021) and then resampled at a 60-meter interval, resulting in the shoreline S_{45} used in the geometric and spectral analysis.

Macroscale – Shape

To measure the shape of the delta, a circle with parameters $\{(x_c, y_c), R_c\}$ was fit to S_{45} using least squares (Jammalamadaka & Sengupta, 2001). The shoreline may correspond only to a sector of a circle, which the least squares fit captures. The center of the circle (x_c, y_c) corresponds to the center of curvature and R_c the radius of curvature. Deltas with a center of curvature lying in the ocean are concave, while those with a center of curvature lying over land are convex. When R_c is significantly larger than the arc length L_C of the circular sector corresponding to the shoreline, the shoreline is essentially flat. That is, when the ratio $L_c/R_c = \varphi$, where φ is the angle of the sector, is smaller than a cutoff φ_{min}, the shoreline is flat. We found that a cutoff $\varphi_{min} = 2\pi/12 = 30°$ clearly separated flat from concave and convex deltas, i.e. if the shoreline corresponds to a circular sector with a radius at least 12 times its length, it is flat.

Mesoscale – Fraction of variance contributed by mouths

To measure the fraction of variance contributed by mouths (fM), first sections of S_{45} corresponding to mouths were identified by denoting which points in S_{45}^R are not a part of S_{90}^R, the shoreline corresponding to a critical angle of $\theta_c = 90°$, i.e. $M_{45}^R = \{(x_i, y_i)|(x_i, y_i) \in S_{45}^R$ and $\notin S_{90}^R\}$. This is because OAM-defined shorelines using different critical angles do not overlap within local concavities (e.g. mouths or embayments). This definition may include embayments such as lagoons sheltered by spits, therefore M_{45}^R was manually inspected and

,

cleaned to represent only mouths. Lastly, the same smoothing procedure used to trans-

form S_{45}^R to S_{45} was used to smooth M_{45}^R and produce M_{45}, which identifies the set of

points in the smoothed shoreline as mouths.

Then to measure what fraction of variability in S_{45} is contributed by M_{45} we used wavelet

analysis to locally estimate the variance in shoreline structure at multiple scales (Kumar

& Foufoula-Georgiou, 1994). For the wavelet analysis a univariate series representing

the shoreline was produced as the distance d_c from every point in S_{45} to the center of

curvature (x_c, y_c), defining a signal $d_c(l)$, where l is the distance along the shoreline. For

convex deltas, the mouths show up as minima, which can be seen in the Mahakam Delta

(Fig. 2). We found that this mapping of the shoreline to a univariate series is preferable

to approaches such as extracting the local curvature series, which is effectively a high-

pass filter removing large scale features and is sensitive to discretization, see Text S3.

Note that mouth widths are typically non-uniform within a delta, resulting in multiscale

variability in the $d_c(l)$ signal, supporting the use of localized analysis of variance in the

spatial domain. Then, the wavelet transform of $d_c(l)$ was computed using the Morlet

wavelet, which has optimal time-frequency localization, with a central frequency of 6

rad/s (Kumar & Foufoula-Georgiou, 1994). The wavelet coefficients are given by $\Psi_{k,l}$ at

a wavenumber (spatial frequency) k and location l along the shoreline, and are used to

estimate the power, $\Psi_{k,l}^2$ (Fig. S2). Finally, the *fM* is defined as the ratio of the integrated

wavelet power for all scales over coefficients corresponding to the mouths, $\Psi_{k,l \in M}$ over the

total power (i.e. variance) of the signal (Eqn. 1), where L is the length of the shoreline

and k_{min} and k_{max} are the minimum and maximum wavenumbers, respectively. Note

,

that typically, wavelet coefficients inside the cone of influence (COI) are excluded from the computation of the variance as they are impacted by edge effects. However, in some deltas the mouths may contain very large features, sometimes spanning over one third of the length of the signal, therefore for all deltas these coefficients were included for more robust estimation of the relative energy in these locations.

$$fM = \int_{k_{min}}^{k_{max}} \int_0^L \Psi_{k,l \in M}^2 \, dl \, dk / \int_{k_{min}}^{k_{max}} \int_0^L \Psi_{k,l}^2 \, dl \, dk. \tag{1}$$

Microscale – Gini-Corrected Fine Scale Variance

Lastly the wavelet transform (Kumar & Foufoula-Georgiou, 1994) was used to estimate the variance at fine scales, i.e. from 300 to 1000 meters (Eqn. 2). Note that here edge effects from the COI can significantly influence the estimated amount of energy at the scales of the features under study, therefore coefficients inside the COI are excluded and the power at each wavenumber k is normalized by the number of points at that frequency, N_k. The sensitivity of the lower bound of 1000 meters was evaluated and no significant changes in the classification were found (Fig. S1).

$$FSV_{1000} = \frac{1}{N_k} \int_{1/1000}^{1/300} \int_0^L \Psi_{k,l}^2 \, dl \, dk. \tag{2}$$

Although two systems may have the same variance at fine scales, one may lack structural variability (i.e. correspond to white noise), while another may have peaks or increased variability at distinct scales. To account for this structured variability, the power spectral density (PSD) of the actual shoreline spatial series is compared to a white noise series with equivalent variance. Specifically, a spectral Gini coefficient g, which measures the total deviation of the cumulative PSD ($cPSD$) from the $cPSD$ of white noise is computed over

,

the fine scales, and used as a multiplier to the FSV_{1000}, defining the $gFSV = g * FSV_{1000}$. This multiplier is low when shoreline variability is similar to white noise, and high when shoreline variability has defined structures (i.e. peaks or higher energy at finer or coarser scales), and helps to separate deltas with similar FSV_{1000} but distinct modes of variability (see Text S2 for details).

All analyses were performed in R using open source geospatial, statistical, and spectral analyses packages (Strimas-Mackey, 2021; Pebesma, 2018, 2021; Pau et al., 2010; Morgan-Wall, 2021; Aybar, 2022; Gouhier et al., 2021).

Sediment Flux Data

Sediment fluxes for every delta were obtained from version 3 of the Nienhuis et al. (2020) database, which used the WBMSed hydrologic model forced with 1981 to 2010 hydroclimate and assuming no human intervention of landscape properties to estimate riverine sediment fluxes, Q_R, (Cohen et al., 2013), angular wave climate data from WaveWatch 3.0 (Chawla et al., 2013) averaged from 1979 to 2009 to estimate wave sediment fluxes, Q_W, and tidal constituents from TXPOv8 inverted from satellite altimetry measurements from 1992 to 2006 (Egbert & Erofeeva, 2002) to estimate tidal sediment fluxes, Q_T. To reduce uncertainty in tidal amplitude estimates associated with the delta outlet location being located too far upstream of the coastline in the global delta database, for all deltas tidal amplitudes from the TXPO grid were obtained at the OAM shoreline extracted at a critical angle 90°. This only resulted in a difference of more than 5 cm for 9 out of 54 deltas, all with significantly widened mouths.

,

Sediment flux data represents a delta-wide value, see (Nienhuis et al., 2020) and references therein for details. For every delta, the relative sediment flux r_x, where x represents either the river, wave, or tide component is defined as:

$$r_x = \frac{Q_x}{Q_R + Q_T + Q_W}. \tag{3}$$

,

Text S2. Spectral Gini Coefficient Definition In order to help separate wave-influenced deltas which are smooth and lack distinct features in the fine scale ranges from the river and tide influenced deltas which contain structure at fine scales, we adjusted the finescale variance by a spectral gini coefficient. To define the spectral gini coefficient and interpert this adjustment, first consider the wavelet-estimated power spectral density, given by Eqn. 4,

$$PSD(k) = \frac{1}{N_k} \int_0^L \Psi_{k,l}^2 dl, \tag{4}$$

where l is the location and k the wavenumber (scale). The spectral variance SV for a range of wavenumbers (scales) k_0 to k_1 is found by integrating with respect to k:

$$SV = \int_{k_0}^{k_1} PSD(k)dk. \tag{5}$$

In general, two signals may have identical SV for a given range of scales but distinct structure. For example, white noise, which by definition has a constant PSD, i.e. $PSD_{WN} = P$, and lacks any structural variability, may have the same SV as a signal with structured variability. To measure the deviation from white noise, consider the normalized PSD, $PSD^*(k)$, given in (Eqn. 6). $PSD^*(k)$ is analogous to a probability density function (PDF), where the integral over the support (i.e. from k_0 to k_1) is 1.

$$PSD^*(k) = \frac{PSD(k)}{SV}. \tag{6}$$

White noise has a uniform spectrum (i.e. flat PSD), while the PSD of another signal may be distributed heterogeneously over the range of wavenumbers (Fig. S2). We then consider the normalized cumulative power spectral density, $cPSD^*(k)$, where k can take

,

on any value up to k_1:

$$cPSD^*(k) = \int_{k_0}^{k} PSD^*(u)du. \tag{7}$$

White noise has a linear $cPSD^*$, while the shoreline $cPSD^*$ is skewed towards relatively coarser scales for $k_0 = \frac{1}{1000}$ m^{-1} and $k_1 = \frac{1}{300}$ m^{-1} (Fig. S2). For these skewed distributions, a natural measure of the deviation from a uniform distribution is the Gini Coefficient, g, which measures the area between the $cPSD^*(k)$ of white noise, $cPSD^*_{WN}(k)$, and the $cPSD^*(k)$ of the shoreline, normalized by the area under the curve of $cPSD^*_{WN}(k)$. As these distribution functions represent spectra this is a spectral Gini Coefficient.

$$g = \frac{\int_{k_0}^{k_1} (cPSD^*_{WN}(k) - cPSD^*(k))dk}{\int_{k_0}^{k_1} cPSD^*_{WN}(k)dk}. \tag{8}$$

The coefficient g increases towards a maximum value of 1 as the PSD is more heterogeneous and approaches zero as the PSD approximates white noise. This coefficient is used as a multiplier to the FSV, computed from $k_0 = \frac{1}{1000}$ m^{-1} to $k_1 = \frac{1}{300}$ m^{-1}, of the shoreline spectra, accounting for the heterogeneous distribution of variance among scales indicative of distinct scale-dependent features (Fig. S2).

,

Text S3. Unsuitability of curvature mapping for shoreline characterization

A common technique to quantitatively analyze meandering rivers is to map the 2D curve corresponding to the channel centerline to a 1D spatial-series represented by its curvature, e.g. (Schwenk et al., 2015), which could also be applied to delta shorelines to perform wavelet analysis. However, for the problem of shoreline characterization we found that the high-pass filter properties of the curvature operator make it unsuitable for extraction of large scale patterns such as channel mouths using spectral analysis. A synthetic example using sinusoids is given to demonstrate these high-pass filter properties. Consider two sinusoids of differing wavenumber with random additive error, $z_1(s) = 5\sin(s) + \mathcal{N}(0, .5)$ and $z_2(s) = 20\sin\left(\frac{s}{2\pi}\right) + \mathcal{N}(0, \ 2)$, along with their sum $z_3(s) = z_2(s) + z_1(s)$ (Fig. S3). The sinusoids represent spatial-series with s being some distance along the shoreline, and are sampled with spatial step $\Delta s = 1$. To analyze the oscillations, the Fourier transform $\hat{z}(k)$ with wavenumber k is taken, with the power spectral density of each signal given in the right panel of (Fig. S3). The additive signal z_3 has clearly defined peaks at $k = (2\pi)^{-1}$ and $k = (2\pi)^{-2}$.

In the case where the functional relationship between z and s is not known, we may want to map the set of coordinates of each $\{(s, z)_i\}$ to a univariate series to employ spectral analysis to characterize the curve. One such common mapping is defining the local curvature κ. For an ordered set of coordinates $\{(x, y)_i\}$ constituting a 2D planar curve, a stable and smooth estimator of the local curvature $\kappa = 1/R$ is given in (Schwenk et al., 2015):

,

$$R = \frac{1}{2} \frac{\sqrt{(\mathbf{a_x^2} + \mathbf{a_y^2})(\mathbf{b_x^2} + \mathbf{b_y^2})(\mathbf{c_x^2} + \mathbf{c_y^2})}}{(\mathbf{a_y b_x} - \mathbf{a_x b_y})}, \tag{9}$$

where $\mathbf{a_x} = x_i - x_{i-1}$, $\mathbf{b_x} = x_{i+1} - x_{i-1}$, $\mathbf{c_x} = x_{i+1} - x_i$. This definition and related curvature operators given in (Schwenk et al., 2015) clearly depend on the sampling resolution of the 2-D planar curve.

The curvature is computed for each curve given by the $\{(s, z)\}$ coordinate pairs to define a univariate series $\kappa(l)$, where l is the distance along the curve (Fig. S4). The noise present in the original signals is amplified by taking local differences and results in the large variation seen in κ_2 and κ_3. The corresponding power spectral density shows that for the high wavenumber series, κ_1, the curvature mapping still captures the wavenumber observed in z_1, but κ_2 and κ_3 have no power near the real wavenumber of $(2\pi)^{-2}$. This is because taking finite differences to compute the curvature filters out the low wavenumber signal.

The sensitivity or ability to capture the low wavenumber signal likely depends on the ratio of the sampling wavenumber $k_s = \Delta s^{-1}$ to the wavenumber of interest k_u, k_s/k_u. By the Nyquist theorem, this ratio must be at least 2 to resolve k_u. When the ratio approaches 2 from a larger value, noise may not be amplified by the curvature transformation, but when it is much larger than 2 noise is amplified. Some value sufficiently optimal to capture k_u using the curvature transformation may exist. However, mouth widths are not constant on deltas and can vary at least by a factor of 2, therefore k_u can vary significantly, so a k_s optimal for the narrowest mouth will amplify noise in the remaining, larger mouths. Moreover, a sufficiently high k_s to capture mouths would filter out information at low

,

wavenumbers, e.g. large scale features such as deltaic lobes. For these reasons the mapping of curvature is not suitable for the problem of shoreline characterization.

References

Aybar, C. (2022). rgee: R bindings for calling the 'earth engine' api [Computer software manual]. Retrieved from `https://CRAN.R-project.org/package=rgee` (R package version 1.1.3)

Baumgardner, S. E. (2016). *Quantifying galloway: Fluvial, tidal and wave influence on experimental and field deltas* (Unpublished doctoral dissertation). University of Minnesota.

Chawla, A., Spindler, D. M., & Tolman, H. L. (2013). Validation of a thirty year wave hindcast using the climate forecast system reanalysis winds. *Ocean Modelling*, *70*, 189–206.

Cohen, S., Kettner, A. J., Syvitski, J., & Fekete, B. M. (2013). Wbmsed, a distributed global-scale riverine sediment flux model: Model description and validation. *Computers & Geosciences*, *53*, 80–93.

Egbert, G. D., & Erofeeva, S. Y. (2002). Efficient inverse modeling of barotropic ocean tides. *Journal of Atmospheric and Oceanic technology*, *19*(2), 183–204.

Galloway, W. E. (1975). Process framework for describing the morphologic and stratigraphic evolution of deltaic depositional system. In *Deltas: Models for exploration* (pp. 87–98). Houston Geological Society.

Geleynse, N., Voller, V., Paola, C., & Ganti, V. (2012). Characterization of river delta shorelines. *Geophysical research letters*, *39*(17).

,

Gouhier, T. C., Grinsted, A., & Simko, V. (2021). R package biwavelet: Conduct univariate and bivariate wavelet analyses [Computer software manual]. Retrieved from `https://github.com/tgouhier/biwavelet` ((Version 0.20.21))

Jammalamadaka, S. R., & Sengupta, A. (2001). *Topics in circular statistics* (Vol. 5). world scientific.

Knights, D., Sawyer, A. H., Barnes, R. T., Piliouras, A., Schwenk, J., Edmonds, D. A., & Brown, A. M. (2020). Nitrate removal across ecogeomorphic zones in wax lake delta, louisiana (usa). *Water Resources Research*, *56*(8), e2019WR026867.

Konkol, A., Schwenk, J., Katifori, E., & Shaw, J. B. (2022). Interplay of river and tidal forcings promotes loops in coastal channel networks. *Geophysical Research Letters*, *49*.

Kumar, P., & Foufoula-Georgiou, E. (1994). Wavelet analysis in geophysics: An introduction. *Wavelets in geophysics*, *4*, 1–43.

Morgan-Wall, T. (2021). rayshader: Create maps and visualize data in 2d and 3d [Computer software manual]. Retrieved from `https://CRAN.R-project.org/package=rayshader` (R package version 0.24.10)

Nienhuis, J. H., Ashton, A. D., Edmonds, D. A., Hoitink, A., Kettner, A. J., Rowland, J. C., & Törnqvist, T. E. (2020). Global-scale human impact on delta morphology has led to net land area gain. *Nature*, *577*(7791), 514–518.

Pau, G., Fuchs, F., Sklyar, O., Boutros, M., & Huber, W. (2010). Ebimage—an r package for image processing with applications to cellular phenotypes. *Bioinformatics*, *26*(7), 979–981. doi: 10.1093/bioinformatics/btq046

,

Pebesma, E. (2018). Simple Features for R: Standardized Support for Spatial Vector Data. *The R Journal*, *10*(1), 439–446. Retrieved from `https://doi.org/10.32614/RJ-2018-009` doi: 10.32614/RJ-2018-009

Pebesma, E. (2021). stars: Spatiotemporal arrays, raster and vector data cubes [Computer software manual]. Retrieved from `https://CRAN.R-project.org/package=stars` (R package version 0.5-5)

Pekel, J.-F., Cottam, A., Gorelick, N., & Belward, A. S. (2016). High-resolution mapping of global surface water and its long-term changes. *Nature*, *540*(7633), 418–422.

Schwenk, J., Lanzoni, S., & Foufoula-Georgiou, E. (2015). The life of a meander bend: Connecting shape and dynamics via analysis of a numerical model. *Journal of Geophysical Research: Earth Surface*, *120*(4), 690–710.

Shaw, J. B., Wolinsky, M. A., Paola, C., & Voller, V. R. (2008). An image-based method for shoreline mapping on complex coasts. *Geophysical Research Letters*, *35*(12).

Strimas-Mackey, M. (2021). smoothr: Smooth and tidy spatial features [Computer software manual]. Retrieved from `https://CRAN.R-project.org/package=smoothr` (R package version 0.2.2)

Vulis, L., Tejedor, A., Zaliapin, I., Rowland, J. C., & Foufoula-Georgiou, E. (2021). Climate signatures on lake and wetland size distributions in arctic deltas. *Geophysical Research Letters*, *48*(20), e2021GL094437.

,
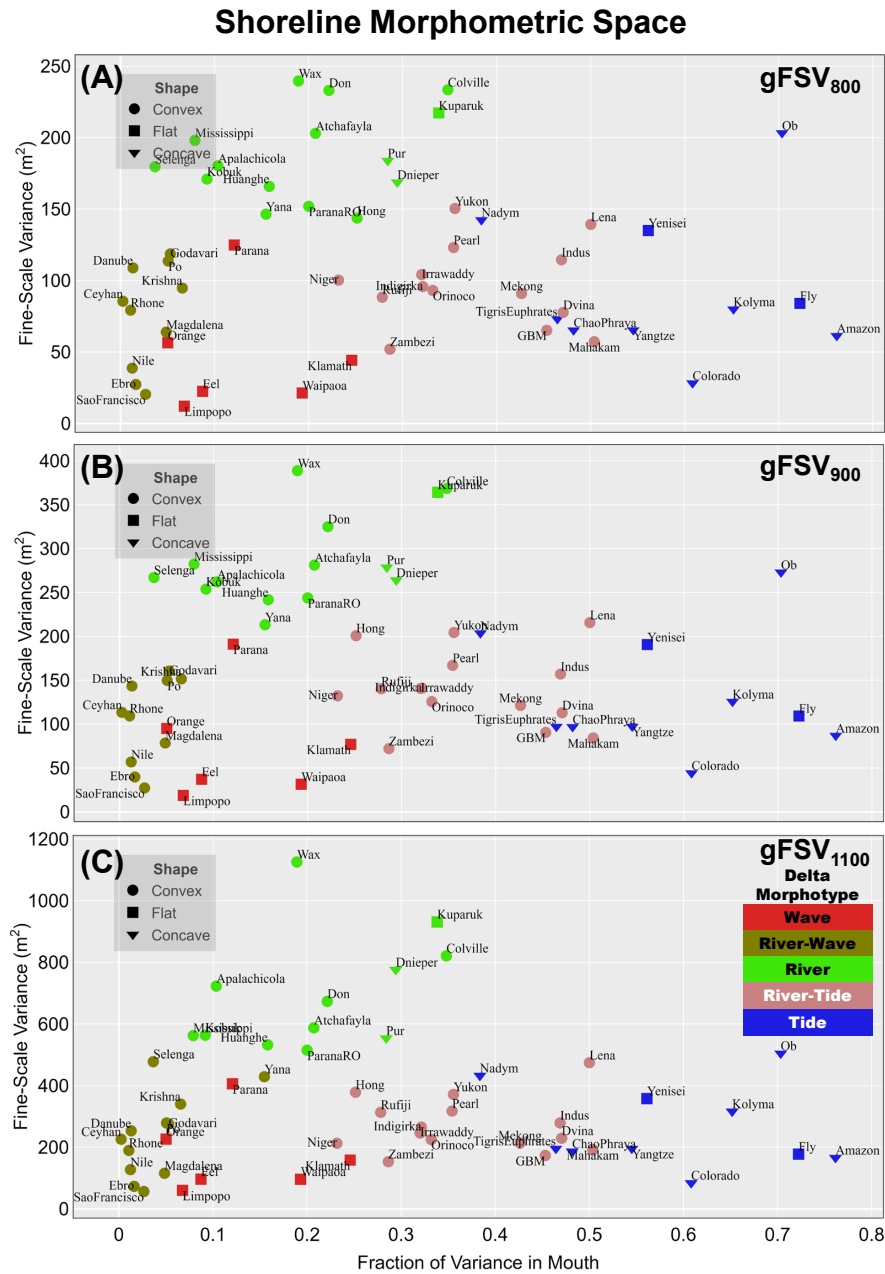
Figure S1. **Insensitivity of the emergent classes to the upper bound of the finescale variance**. There is almost no discernible difference in the deltas belonging to each emergent morphotype when adjusting the upper wavelength of the Gini-corrected Fine Scale Variance ($gFSV$) between 800 m to 1100 m. Only the Selenga and Yana switch from the river morphotype to river-wave morphotype for an upper wavelength of 1100 m, but lay on the boundary of the two classes.

(A)

(B)
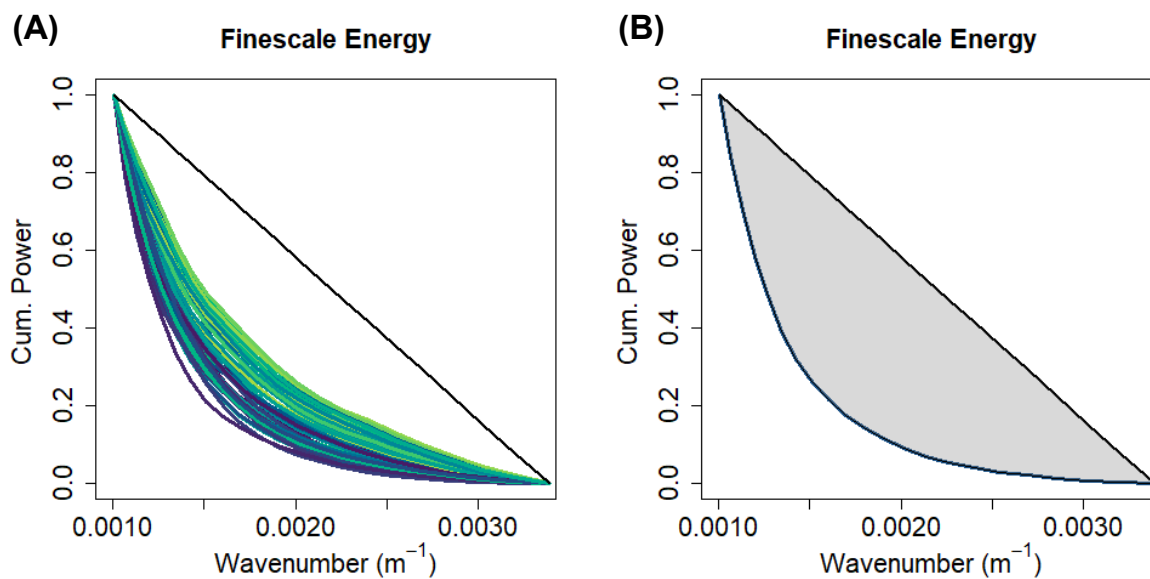
Figure S2.   **Cumulative Power Spectral Density ($cPSD^*$) of the shoreline signals.** (A) The $cPSD^*$ curves of the 54 analyzed delta shorelines, each normalized to have a value of one over the fine scales. The straight black line is $cPSD^*_{WN}$ and overlaps for each delta due to the normalization to have unit power. (B) Example of the deviation between an arbitrarily selected real shoreline and white noise with equivalent energy. The Gini Coefficient (g) is the area between the two curves normalized by the area under the white noise.
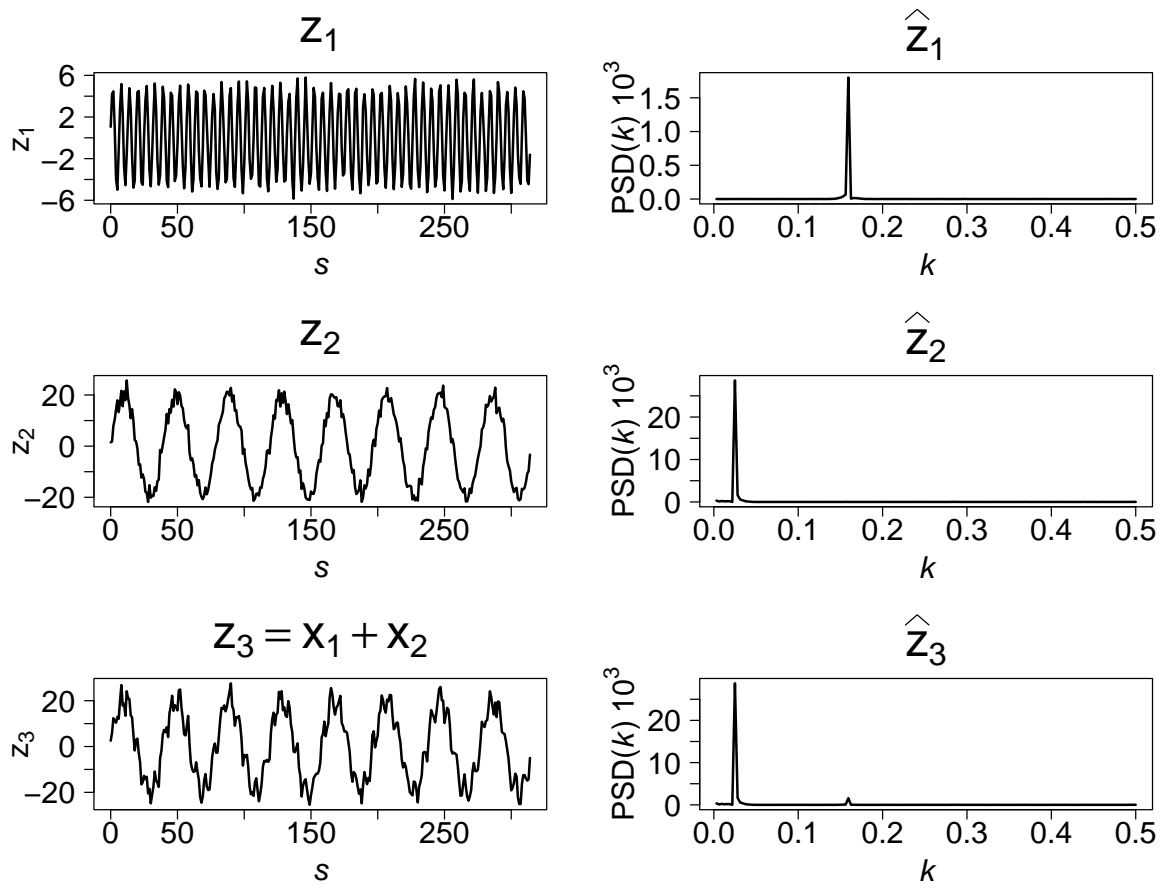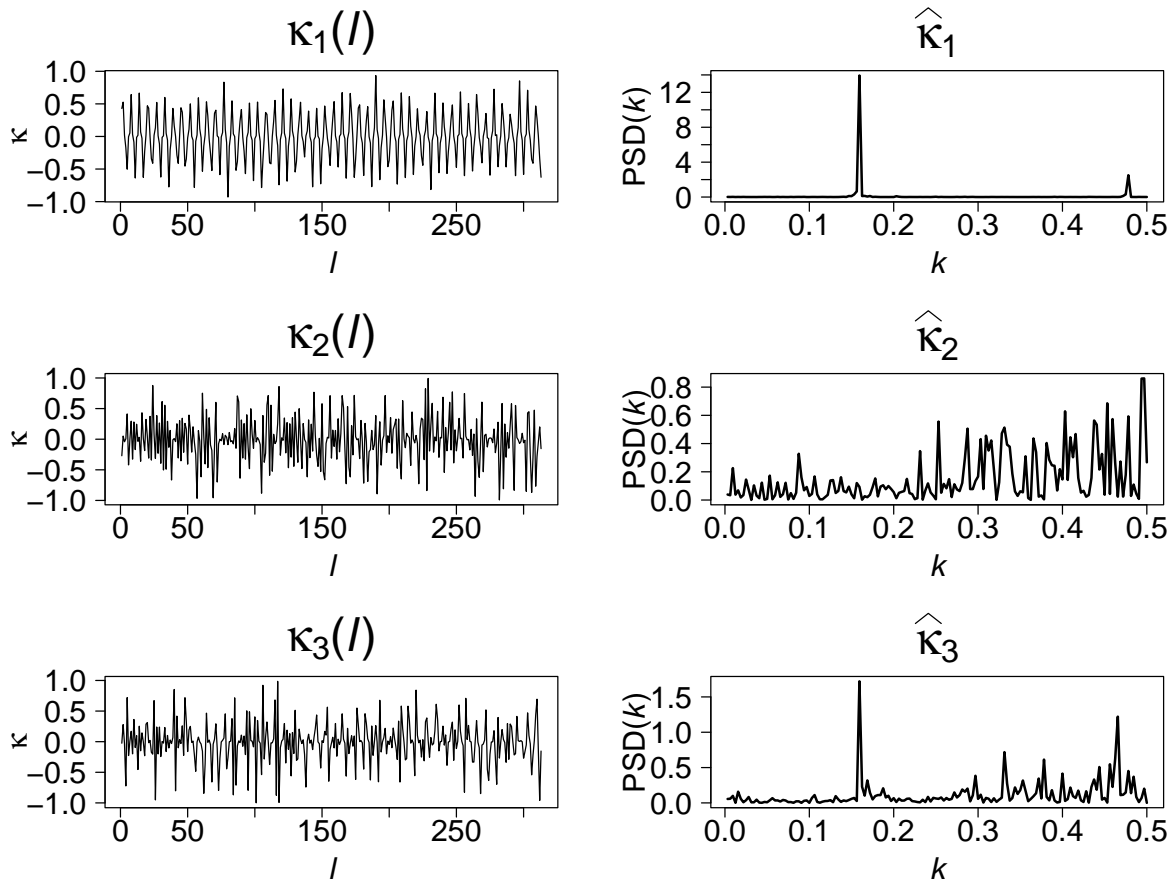
,

Figure S3. Synthetic sinusoids and their corresponding power spectral density.

,

Figure S4.   Result of the curvature operator on sinusoids. The sinusoids from

Fig. S3 transformed to curvature spatial-series using Equation (9). Note that κ_2 and κ_3

fail to capture the low frequency signal present in z_2 and z_3.